Supplement of Atmos. Chem. Phys., 25, 8185–8211, 2025
https://doi.org/10.5194/acp-25-8185-2025-supplement

Atmospheric Chemistry and Physics
Open Access
EGU

Supplement of

Advances in characterization of black carbon particles and their associated coatings using the soot-particle aerosol mass spectrometer in Singapore, a complex city environment

Mutian Ma et al.

Correspondence to: Alex King Yin Lee (alex.lee@ec.gc.ca)

ToF-ACSM data analysis

The chemical characterization of NR-PM1 was obtained by a time-of-flight aerosol chemical speciation monitor (ToF-ACSM. Aerodyne Research Inc.) in 1-minute time resolution. A full description of the instrument can be found in Fröhlich et al. (2013). Similarly to the SP-AMS, it is composed of an aerodynamic lens that focuses the particle beam and directs it through three vacuum chambers, the last one being a detection chamber in which particles are vaporized by impaction on a Tungsten vaporizer heated at 600 ◦C and then ionized by electron impact (70 eV). Particles are then detected by the time of flight mass spectrometer. The ToF-ACSM data were processed by the Tofware (v3.2.4, Tofwerk AG, Thun, Switzerland). The ionization efficiency (IE) of nitrate and relative ionization efficiency (RIE) of ammonium and sulfate were calibrated before and after the measurement. The calculated and default RIE values of NO_3^- (1.1), SO_4^{2-} (0.46), Cl^- (1.3), Org (1.4), and NH_4^+ (3.14) were used to quantify NR-PM1.

Size distribution of rBC and associated coating materials

Figure S11 presents the size distributions of rBC and the major species of NR-$PM_{coating}$ (i.e., OA, NO_3^-, and SO_4^{2-}). rBC mass peaked at around 180 nm, and its concentration gradually decreased as a function of particle size. In this work, the majority of rBC-containing particle was emitted by local combination sources without substantial degree of atmospheric aging, which is supported by the results of source apportionment analysis (see Section 3.3-3.5) that ~81% of rBC was emitted from local traffic and industrial emissions. Bimodal distribution was clearly observed for OA, and the intensities of peaks at ~200 nm and 465 nm are comparable. This implies that OA in NR-$PM_{coating}$ were influenced significantly by both primary and secondary sources, which is consistent with the results of source apportionment analysis that ~41% and 49% of OA in NR-$PM_{coating}$ was due to local primary emissions and SOA, respectively. NO_3^-, and SO_4^{2-} peaked between 500 and 600 nm, suggesting that most of these IA species were associated with more aged rBC-containing particles. Nevertheless, a weaker peak of NO_3^-, and SO_4^{2-} at ~200 nm highlights that these IA might condense on freshly emitted rBC in a relatively short time scale when they were locally formed via photochemistry. The details of source apportionment results based on different PMF scenarios will be discussed in Section 3.3.

The size distributions of some fragment ions, including m/z 43, 44, 55, 57, and 60, are shown in Fig. S10b, and most of them also had bimodal distributions. Signals of m/z 43, 55, and 57 could be significantly contributed by both $C_xH_y^+$ and $C_xH_yO_z^+$ fragments from OA, but their relative contributions across different particle size cannot be resolved by the unit mass resolution (UMR) data. Although m/z 60 can be mainly contributed by C_5^+ from rBC and $C_2H_4O_2^+$ from OA (i.e., the biomass burning tracer organic fragment), the size distribution of rBC, m/z 39 (K^+) and m/z 213 ($K_3SO_4^+$) (Fig. S10b-c) suggests that biomass burning-influenced rBC-containing particles observed in this work had relatively large particle size and $C_2H_4O_2^+$ is likely the key contributor to the m/z 60 signals within the larger size range.

ToF-ACSM PMF analysis

PMF analysis of OA measured by ACSM was performed by the Source Finder (SoFi, version 8) and ME-2 solver as described previously (Canonaco et al., 2013). Up to 10-factor solution was evaluated following the same approach as for SP-AMS PMF. A 4-factor solution was selected (referred as PMF_{ACSM}, Fig. S13). The four factors include HOA, cooking-related OA (COA), BBOA, and OOA. The subscript of ACSM indicates the PMF factors (i.e., HOA_{ACSM}) identified by ACSM measurements in the subsequent discussion. The mass spectral profiles, diurnal patterns, NWR plots, and PSCF plots of these four factors are reported in Fig. S13.

Coating Thickness Estimation

Assuming the particles are spherical, the coating thickness of rBC-containing particles were estimated using the following equation. The relative density of OA and BC used in the estimation were 1.2 and 1.8 (El Mais et al., 2023; Fan et al., 2020), respectively.

$$t_{coat} = r_{part} - \sqrt[3]{(\frac{\rho_{coat} * r_{part}^3}{R * \rho_{core} + \rho_{coat}})}$$ [1]

where t_{coat} is the coating thickness, r_{part} is the particle radius, ρ_{core} and ρ_{coat} are the density of rBC and OA, respectively, R is the OA-to-rBC ratio (Org/rBC).

The estimations of coating thickness at different particle sizes (100, 300 and 600 nm) are summarized in Table S2 as illustration. For example, an Org/BC ratio of 1 for a 100 nm particle will result in an estimated coating thickness of 13.2 nm, contributing to 26.3% of the overall particle diameter. The percentage contribution of coating to the overall particle diameter is a function of Org/rBC ratio at a given particle size. It is important to note that bare/fresh BC particles (i.e., low Org/rBC ratio), they are likely to be more fractal (Wang et al., 2021) which would lead to overestimation of the coating thickness.

Table S1. Detection limit for metal and metal ions.

Metal/metal salt	**Na^+**	**K^+**	**Rb^+**	**V^+**	**Ni^+**	**$K_3SO_4^+$**
Detection limit (Hz)	7.33	40.36	0.52	0.50	0.35	0.23
Campaign average (Hz)	26.70	500.20	1.85	1.74	0.64	5.16

Table S2. Coating thickness calculation for different particle sizes and Org/rBC ratios.

Particle size (nm)	**Org/rBC**	**Coating thickness (nm)**	**Coating thickness (%)**
100	0.1	2.3	4.6%
100	1	13.2	26.3%
100	10	30.2	60.3%
300	0.1	6.8	4.6%
300	1	39.5	26.3%
300	10	90.5	60.3%
600	0.1	13.7	4.6%
600	1	79.0	26.3%
600	10	180.9	60.3%

Table S3. The Org/rBC ratios for factors identified by PMF_{base-4}, $PMF_{metal-7}$ and PMF_{all-8}

	PMF_{base-4}	**$PMF_{metal-7}$**	**PMF_{all-8}**
HOA	6.6	11.3	13.9
rBC-rich*	0.1	0.1	0.1
LO-OOA	61.0	17.8	18.3
MO-OOA	6.8	9.4	7.4
IOA*	NA	0.2	0.2
BBOA	NA	2.8	3.7
A-BBOA	NA	2.8	6.9
Night-IA-BBOA	NA	NA	2.3

*All CO^+, CO_2^+ and $C_3O_2^+$ signals are considered as rBC mass as rBC-rich and IOA are largely dominated by rBC mass.

Table S4. Mass spectra and time series correlations of $PMF_{base\text{-}4}$ factors against to those from $PMF_{metal\text{-}4}$ and $PMF_{all\text{-}4}$.

	Mass spectra correlations with $PMF_{base\text{-}4}$ ($R_{m/z}$)				**Time series correlations (R_{ts}) with $PMF_{base\text{-}4}$**			
PMF factors	**HOA**	**rBC-rich**	**LO-OOA**	**MO-OOA**	**HOA**	**rBC-rich**	**LO-OOA**	**MO-OOA**
HOA $_{metal\text{-}4}$	**1.00**	0.38	0.40	0.24	**0.96**	0.78	0.52	0.07
rBC-rich $_{metal\text{-}4}$	0.41	**1.00**	0.44	0.77	0.78	**0.94**	0.45	0.04
LO-OOA $_{metal\text{-}4}$	0.34	0.54	**0.98**	0.89	0.42	0.38	**0.97**	0.70
MO-OOA $_{metal\text{-}4}$	0.25	0.80	0.75	**1.00**	0.03	0.00	0.47	**0.97**
HOA $_{all\text{-}4}$	**1.00**	0.44	0.41	0.28	**1.00**	0.79	0.52	0.07
rBC-rich $_{all\text{-}4}$	0.43	**1.00**	0.46	0.78	0.71	**0.98**	0.37	0.01
LO-OOA $_{all\text{-}4}$	0.35	0.56	**0.98**	0.89	0.45	0.41	**0.99**	0.66
MO-OOA $_{all\text{-}4}$	0.25	0.79	0.77	**1.00**	0.03	-0.01	0.48	**0.98**

Table S5. Mass spectra and time series correlations of $PMF_{metal-7}$ factors against to those from $PMF_{metal-4}$.

		Mass spectra correlations ($R_{m/z}$)						
PMF solution		**HOA**	**rBC-rich**	**LO-OOA**	**MO-OOA**	**IOA**	**A-BBOA**	**BBOA**
HOA	**Slope**	1.06	0.84	0.48	0.31	0.79	0.47	0.54
	R	**0.99**	0.35	0.50	0.24	0.48	0.28	0.50
rBC-rich	**Slope**	0.14	1.05	0.09	0.17	0.71	0.30	0.37
	R	0.24	**1.00**	0.17	0.34	0.98	0.42	0.80
LO-OOA	**Slope**	0.50	0.80	0.93	1.08	0.68	0.69	0.67
	R	0.34	0.29	**0.94**	0.94	0.35	0.37	0.55
MO-OOA	**Slope**	0.35	1.23	0.56	0.86	0.91	1.24	0.88
	R	0.25	0.54	0.60	**0.84**	0.57	0.83	0.88

		Time series correlations (R_{ts})						
PMF solution		**HOA**	**rBC-rich**	**LO-OOA**	**MO-OOA**	**IOA**	**A-BBOA**	**BBOA**
HOA	**Slope**	0.46	0.63	0.23	0.21	0.22	0.07	0.14
	R	**0.99**	0.71	0.58	0.10	0.68	0.05	0.27
rBC-rich	**Slope**	0.27	0.50	0.15	0.15	0.13	0.05	0.10
	R	0.77	**0.97**	0.49	0.07	0.61	0.03	0.23
LO-OOA	**Slope**	0.31	0.48	0.32	0.51	0.16	0.12	0.22
	R	0.40	0.32	**0.92**	0.78	0.36	0.48	0.61
MO-OOA	**Slope**	0.14	0.25	0.14	0.49	0.07	0.14	0.21
	R	0.01	-0.03	0.30	**0.94**	0.06	0.92	0.80

Table S6. Mass spectra and time series correlations of PMF_{all-8} factors against to those from PMF_{all-4}.

		Mass spectra correlations ($R_{m/z}$)							
PMF solution		**HOA**	**rBC-rich**	**LO-OOA**	**MO-OOA**	**IOA**	**A-BBOA**	**BBOA**	**Night-IA-BBOA**
HOA	**Slope**	1.04	0.43	0.40	0.29	0.47	0.29	0.43	0.35
	R	**0.97**	0.16	0.42	0.24	0.26	0.13	0.38	0.24
rBC-rich	**Slope**	0.36	1.45	0.34	0.52	1.08	0.68	0.72	0.61
	R	0.35	**0.75**	0.43	0.62	0.79	0.48	0.85	0.60
LO-OOA	**Slope**	0.49	0.44	0.93	0.98	0.43	0.49	0.56	0.58
	R	0.33	0.13	**0.96**	0.88	0.18	0.22	0.43	0.38
MO-OOA	**Slope**	0.31	0.44	0.65	0.91	0.42	1.08	0.70	0.61
	R	0.19	0.15	0.69	**0.88**	0.20	0.61	0.62	0.44

		Time series correlations (R_{ts})							
PMF solution		**HOA**	**rBC-rich**	**LO-OOA**	**MO-OOA**	**IOA**	**A-BBOA**	**BBOA**	**Night-IA-BBOA**
HOA	**Slope**	0.41	0.50	0.22	0.17	0.21	0.03	0.11	0.10
	R	**0.99**	0.69	0.58	0.06	0.68	0.06	0.28	0.09
rBC-rich	**Slope**	0.29	0.50	0.17	0.15	0.15	0.04	0.10	0.10
	R	0.70	**0.96**	0.43	0.01	0.53	0.06	0.23	0.10
LO-OOA	**Slope**	0.29	0.40	0.33	0.44	0.16	0.06	0.19	0.11
	R	0.43	0.32	**0.94**	0.68	0.36	0.44	0.67	0.21
MO-OOA	**Slope**	0.12	0.20	0.14	0.49	0.07	0.08	0.19	0.10
	R	-0.01	-0.04	0.28	**0.96**	0.07	0.88	0.86	0.26

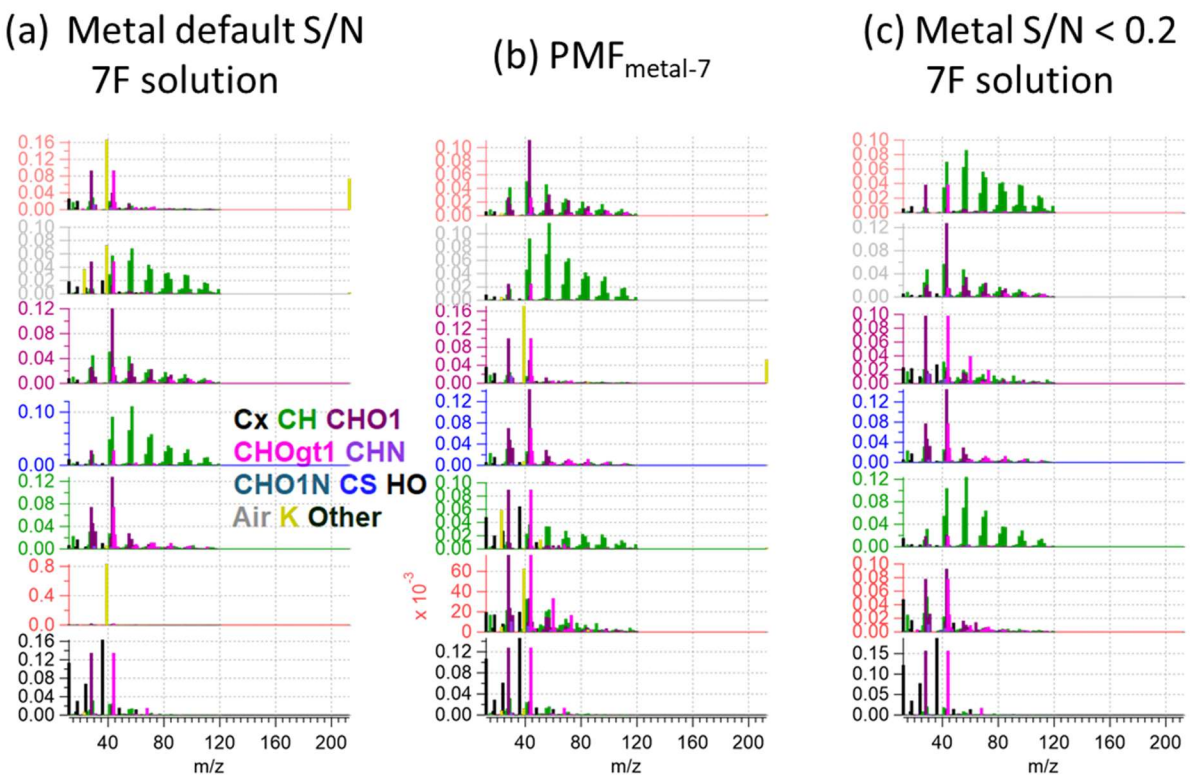

Figure S1. The comparison of 7-factor solutions using default S/N with K^+ dominated factor (i.e., poor separation, a), adjusted S/N in $PMF_{metal\text{-}7}$ (b), and over-adjusted S/N showing over-separation (i.e., S/Ns < 0.2, c).

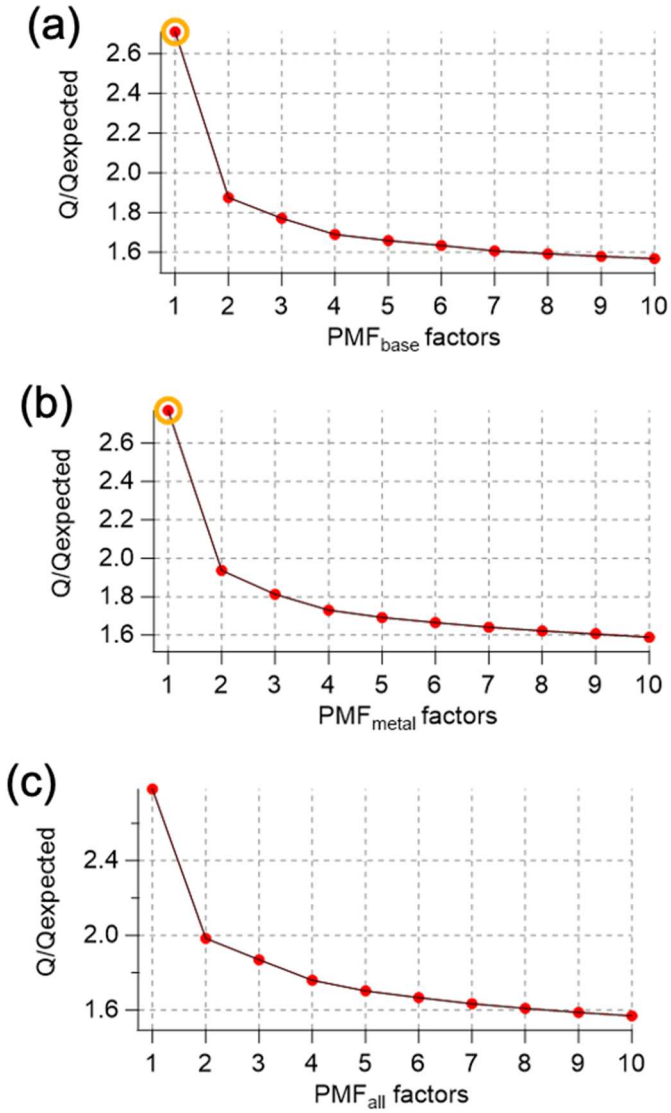

Figure S2. $Q/Q_{expected}$ plots for different PMF scenarios up to 10-factor solution.

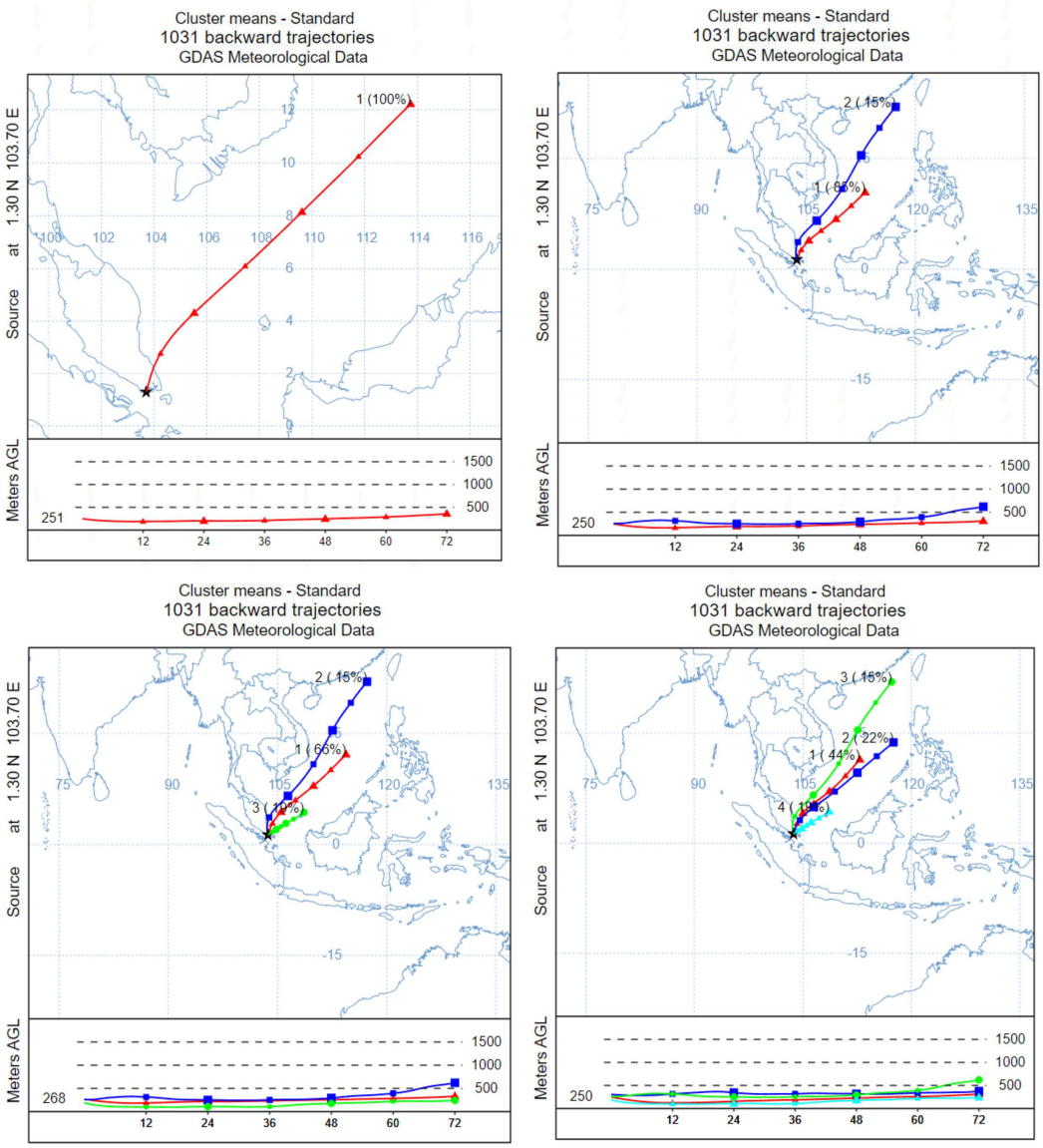

Figure S3. Results of cluster analysis (from 1 to 4 clusters) of 72-hours air mass back trajectory.

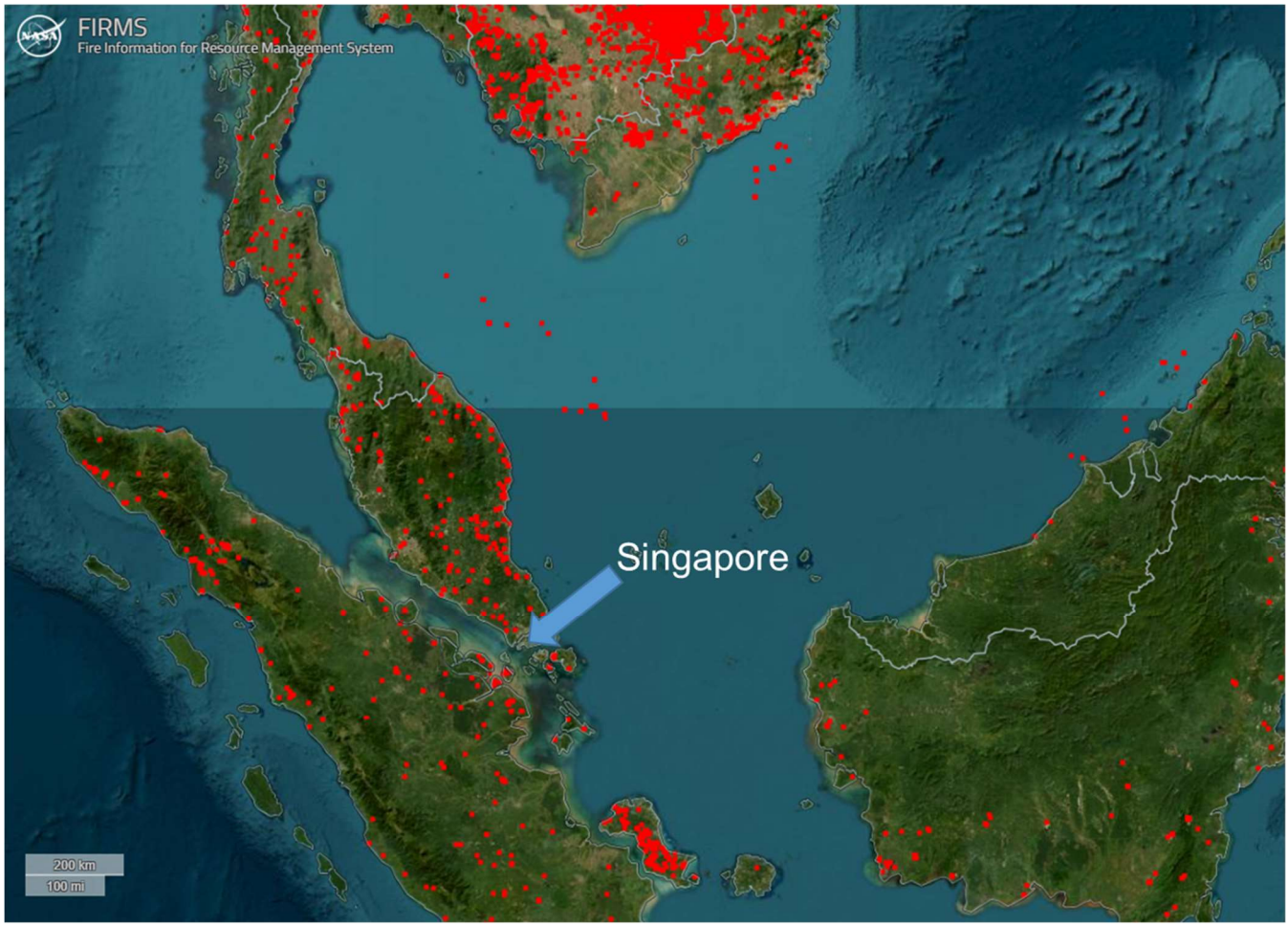

Figure S4. Regional fire counts from 2022/01/22-2022/01/29 (red dots in the map, https://firms.modaps.eosdis.nasa.gov/map/).

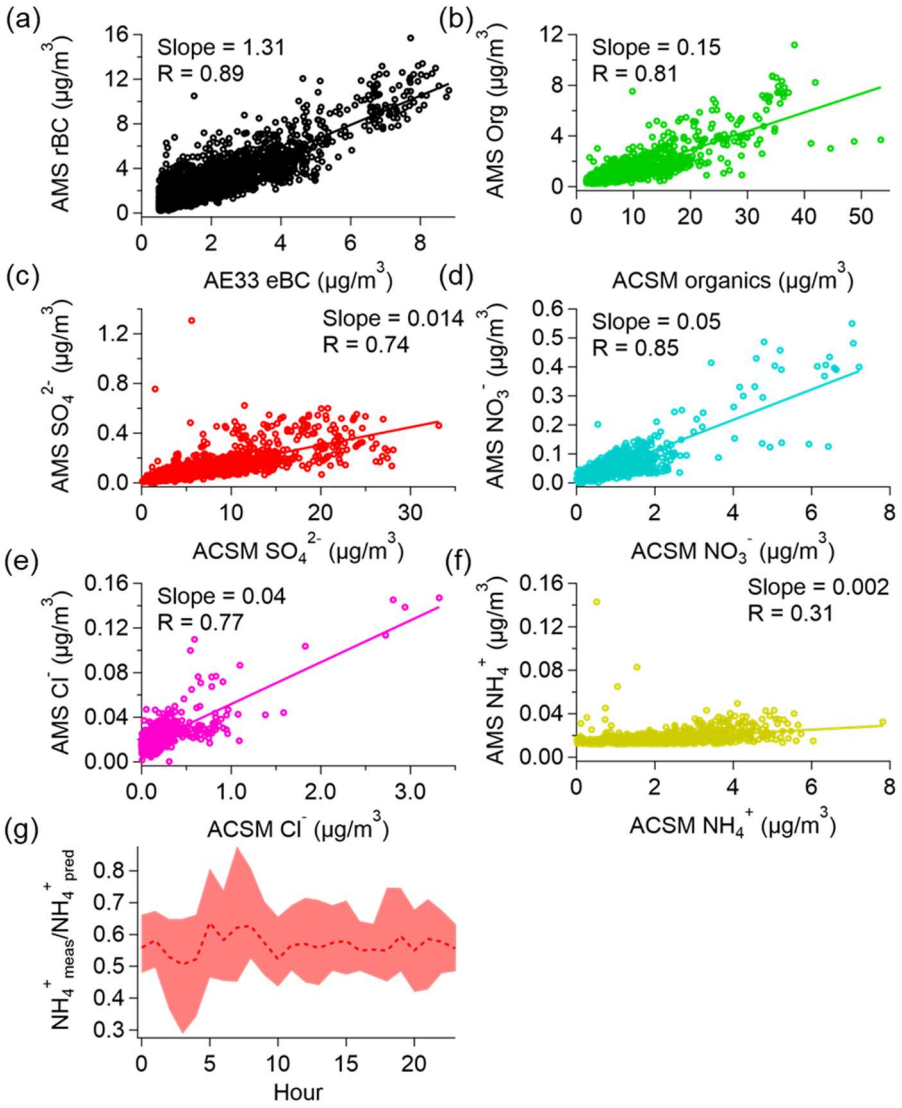

Figure S5. Time series correlation of chemical species between bulk SP-AMS measurements and aethalometer (a) and ToF-ACSM (b-f) measurements. (g) $NH4^{+}_{meas}$ / $NH4^{+}_{pred}$ of NR-PM_1

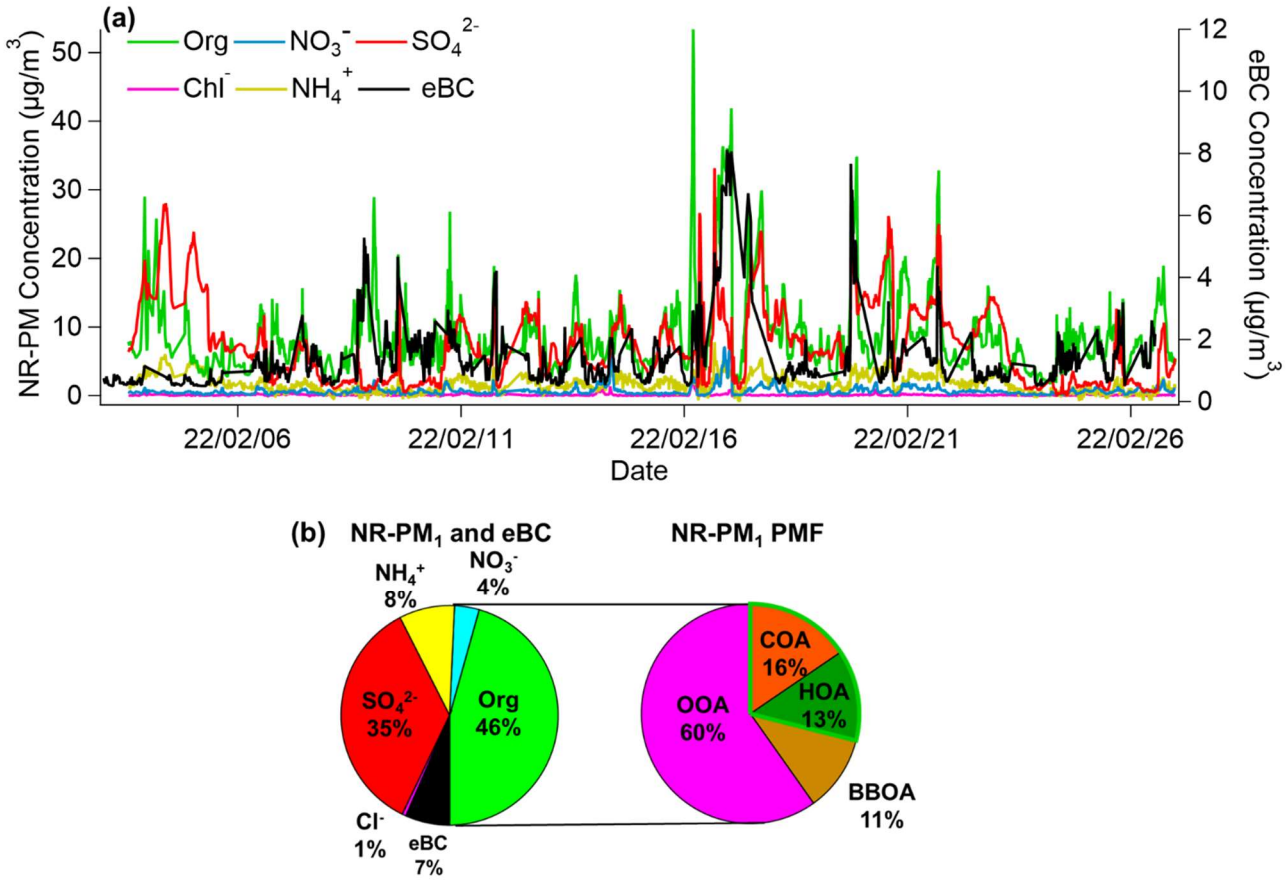

Figure S6. (a) Timeseries of NR-PM_1 measured by the ToF-ACSM and eBC measured by the aethalometer. (b) Mass fraction contribution of NR-PM_1 and eBC (left) and OA factors identified in NR-PM_1.

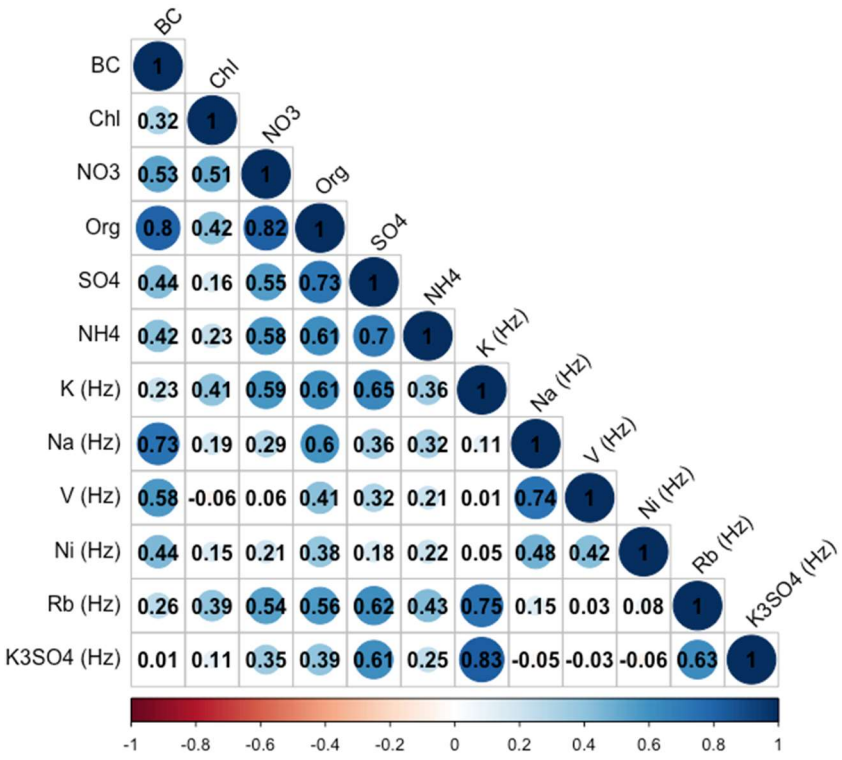

Figure S7. Pearson correlation (R) values are shown in corresponding cells. The R values are also shown by the size and color of the circle in the cells.

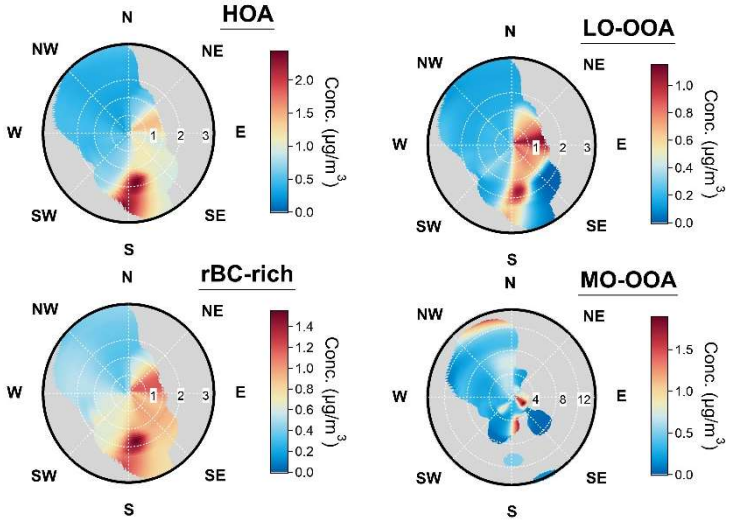

Figure S8. The NWR plots of factors identified by $PMF_{base\text{-}4}$ with different wind speed ranges (< 3 m/s) and resolution than Figure 7.

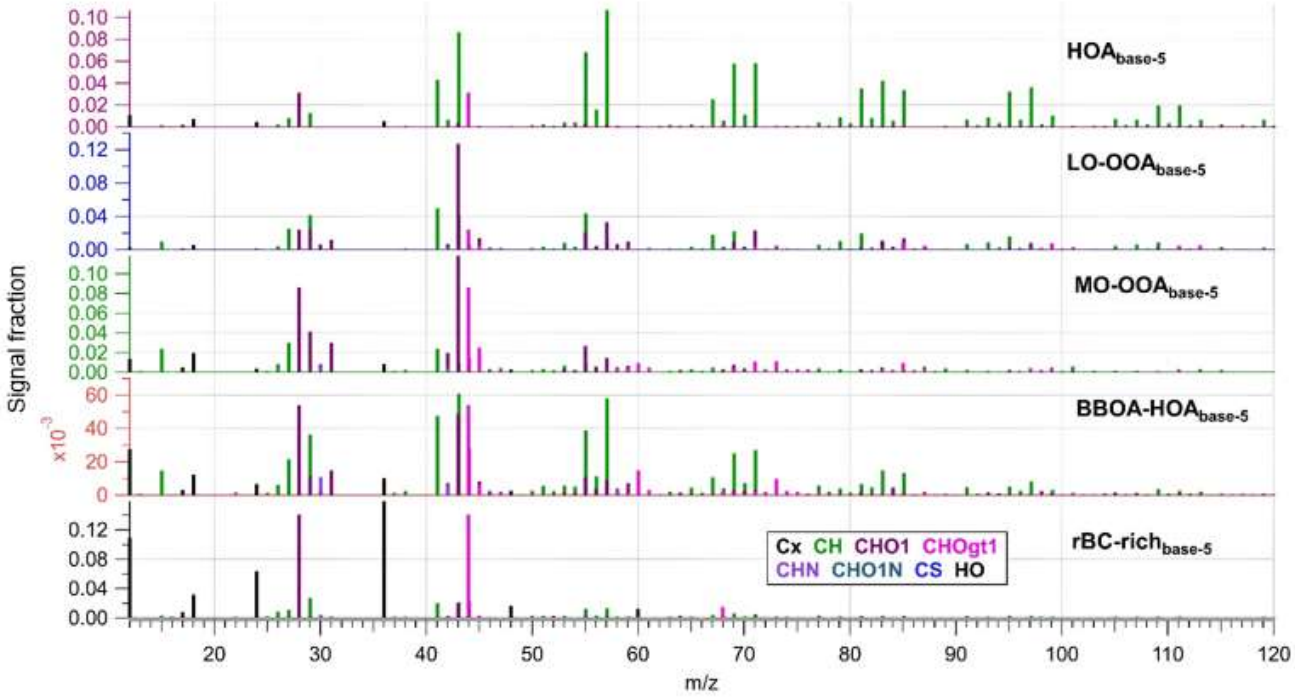

Figure S9. Summary of the 5-factor solutions of PMF_{base}.

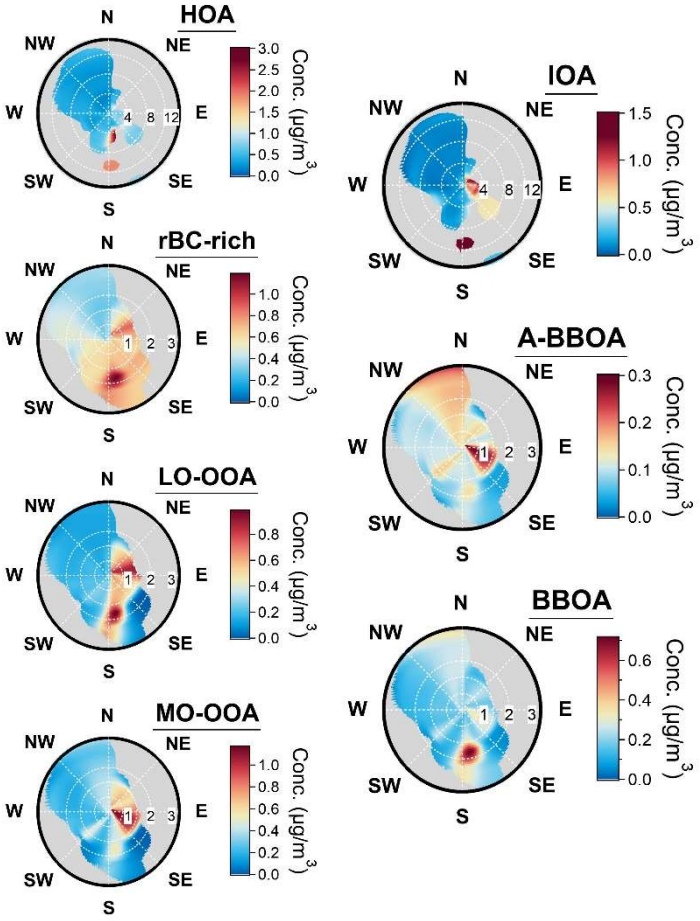

Figure S10. The NWR plots of factors identified by $PMF_{metal-7}$.

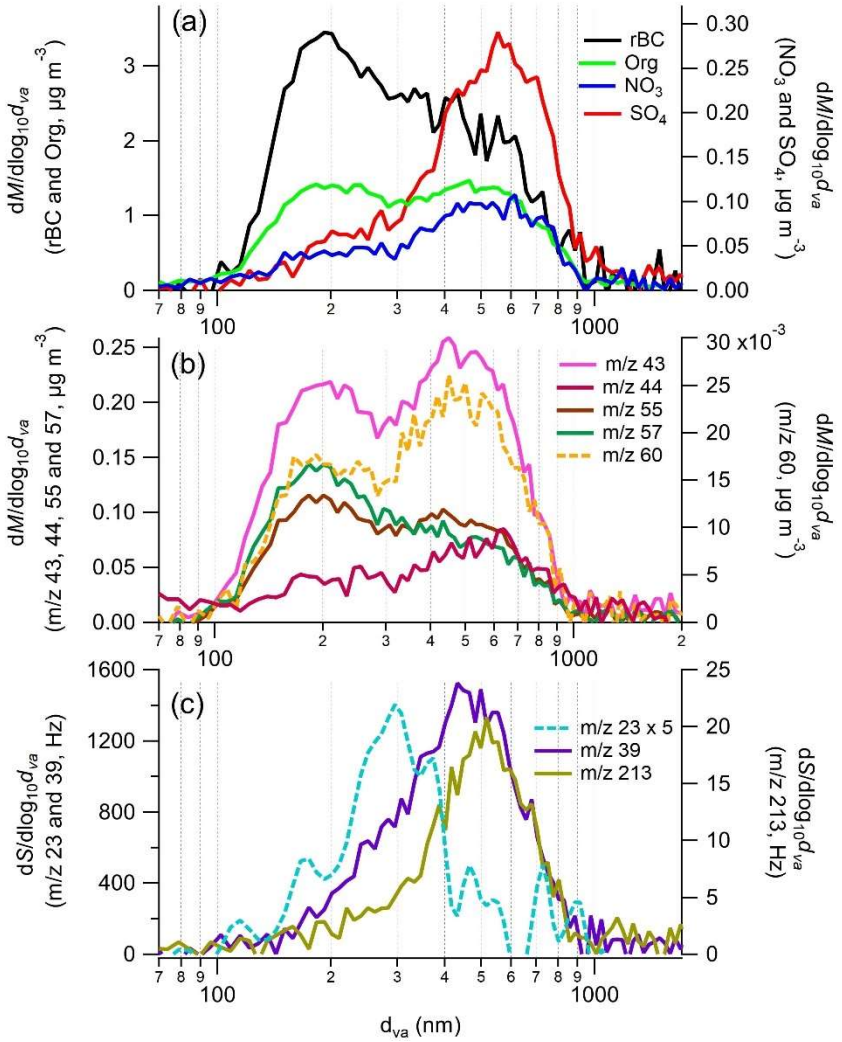

Figure S11: Size distribution of rBC and associated coating materials. Signals at m/z 43, 44, 55, 55, and 60 were converted to mass concentrations of organics assuming they are mainly contributed by OA. Signals at m/z 23, 39 and 213 are used to represent Na^+, K^+ and $K_3SO_4^+$, respectively. Signals at m/z 23 were smoothed and multiplied by a factor of 5.

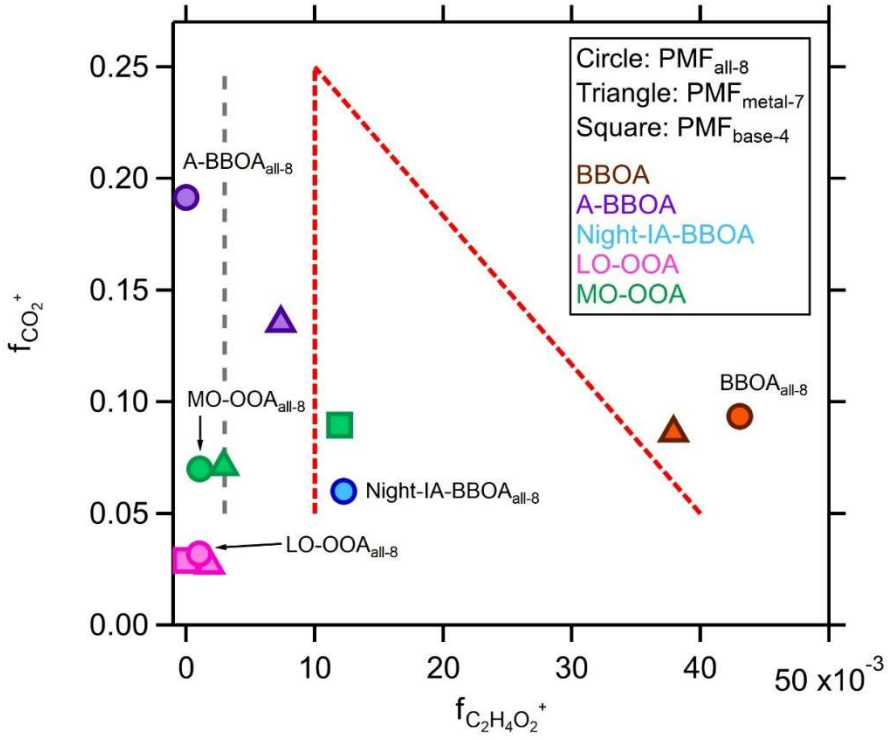

Figure S12. The $f_{CO_2^+}$ vs. $f_{C_2H_4O_2^+}$ plot for evaluating OOA and biomass burning-related OA factors derived from different PMF scenarios. Correction factor was not applied for $f_{C_2H_4O_2^+}$ in this plot. Grey dashed line represents background level (0.3%) of $f_{C_2H_4O_2^+}$ for OA without significant biomass burning signature reported by Cubison et al. (2011). Red dashed lines represent the boundaries of triangular region that cover BBOA observed by Cubison et al. (2011).

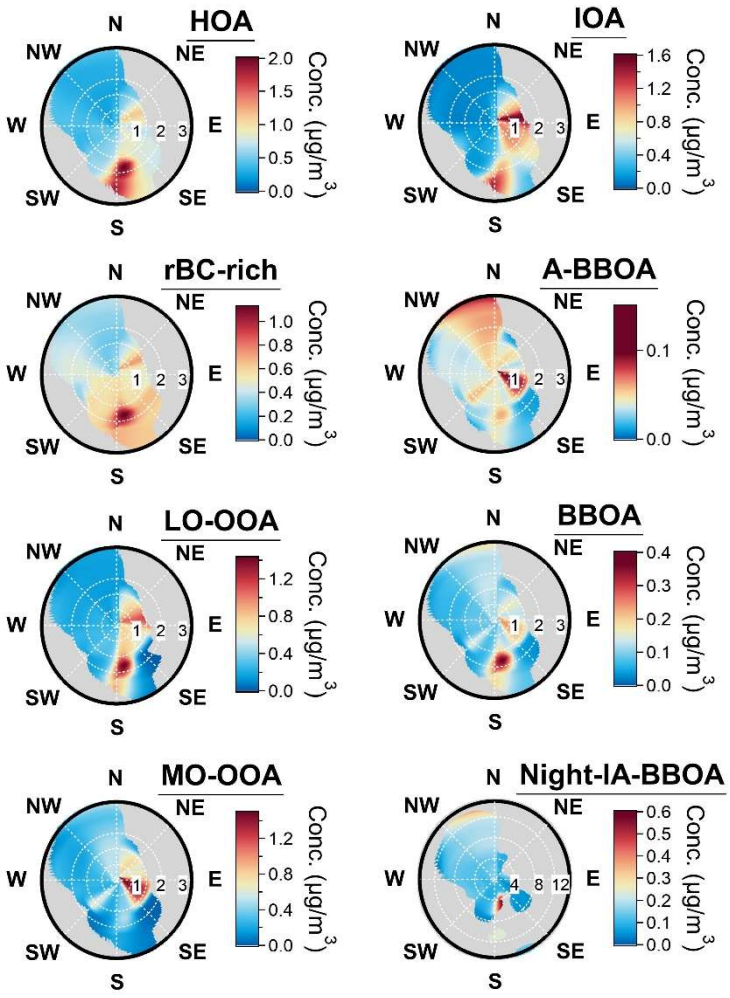

Figure S13. The NWR plots of factors identified by $PMF_{all\text{-}8}$.

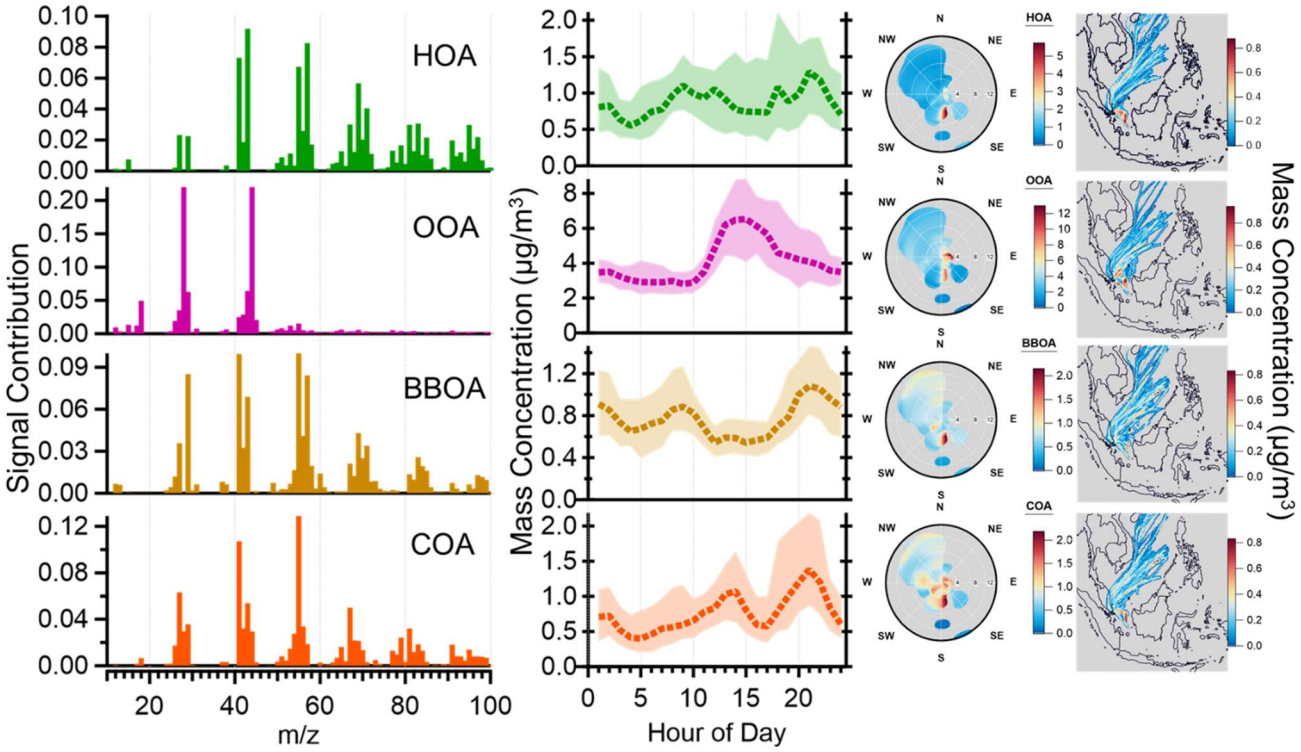

Figure S14. The mass spectral profiles, diurnal patterns, NWR plots and 4-factor PMF solution of ACSM and their corresponding diurnal patterns.

Reference

Canonaco, F., Crippa, M., Slowik, J. G., Baltensperger, U., and Prévôt, A. S. H.: SoFi, an IGOR-based interface for the efficient use of the generalized multilinear engine (ME-2) for the source apportionment: ME-2 application to aerosol mass spectrometer data, Atmos. Meas. Tech., 6, 3649-3661, 10.5194/amt-6-3649-2013, 2013.

Cubison, M. J., Ortega, A. M., Hayes, P. L., Farmer, D. K., Day, D., Lechner, M. J., Brune, W. H., Apel, E., Diskin, G. S., Fisher, J. A., Fuelberg, H. E., Hecobian, A., Knapp, D. J., Mikoviny, T., Riemer, D., Sachse, G. W., Sessions, W., Weber, R. J., Weinheimer, A. J., Wisthaler, A., and Jimenez, J. L.: Effects of aging on organic aerosol from open biomass burning smoke in aircraft and laboratory studies, Atmos. Chem. Phys., 11, 12049-12064, 10.5194/acp-11-12049-2011, 2011.

El Mais, A. E. R., D'Anna, B., Drinovec, L., Lambe, A. T., Peng, Z., Petit, J. E., Favez, O., Aït-Aïssa, S., and Albinet, A.: Insights into secondary organic aerosol formation from the day- and nighttime oxidation of polycyclic aromatic hydrocarbons and furans in an oxidation flow reactor, Atmos. Chem. Phys., 23, 15077-15096, 10.5194/acp-23-15077-2023, 2023.

Fan, X., Liu, J., Zhang, F., Chen, L., Collins, D., Xu, W., Jin, X., Ren, J., Wang, Y., Wu, H., Li, S., Sun, Y., and Li, Z.: Contrasting size-resolved hygroscopicity of fine particles derived by HTDMA and HR-ToF-AMS measurements between summer and winter in Beijing: the impacts of aerosol aging and local emissions, Atmos. Chem. Phys., 20, 915-929, 10.5194/acp-20-915-2020, 2020.

Fröhlich, R., Cubison, M. J., Slowik, J. G., Bukowiecki, N., Prévôt, A. S. H., Baltensperger, U., Schneider, J., Kimmel, J. R., Gonin, M., Rohner, U., Worsnop, D. R., and Jayne, J. T.: The ToF-ACSM: a portable aerosol chemical speciation monitor with TOFMS detection, Atmos. Meas. Tech., 6, 3225-3241, 10.5194/amt-6-3225-2013, 2013.

Wang, Y., Pang, Y., Huang, J., Bi, L., Che, H., Zhang, X., and Li, W.: Constructing Shapes and Mixing Structures of Black Carbon Particles With Applications to Optical Calculations, J. Geophys. Res.: Atmos., 126, e2021JD034620, https://doi.org/10.1029/2021JD034620, 2021.